

# Latent Generative Solvers for Generalizable Long-Term Physics Simulation

Zituo Chen<sup>1</sup> Haixu Wu<sup>2</sup> Sili Deng<sup>1</sup>

## Abstract

We study long-horizon surrogate simulation across heterogeneous PDE systems. We introduce Latent Generative Solvers (LGS), a two-stage framework that (i) maps diverse PDE states into a shared latent physics space with a pretrained VAE, and (ii) learns probabilistic latent dynamics with a Transformer trained by flow matching. Our key mechanism is an uncertainty knob that perturbs latent inputs during training and inference, teaching the solver to correct off-manifold rollout drift and stabilizing autoregressive prediction. We further use flow forcing to update a system descriptor (context) from model-generated trajectories, aligning train/test conditioning and improving long-term stability. We pretrain on a curated corpus of  $\sim 2.5M$  trajectories at  $128^2$  resolution spanning 12 PDE families. LGS matches strong deterministic neural-operator baselines on short horizons while substantially reducing rollout drift on long horizons. Learning in latent space plus efficient architectural choices yields up to **70 $\times$**  lower FLOPs than non-generative baselines, enabling scalable pretraining. We also show efficient adaptation to an out-of-distribution  $256^2$  Kolmogorov flow dataset under limited finetuning budgets. Overall, LGS provides a practical route toward generalizable, uncertainty-aware neural PDE solvers that are more reliable for long-term forecasting and downstream scientific workflows.

## 1. Introduction

Neural PDE solvers aim to learn surrogate operators for partial differential equations (PDEs) that generalize across initial conditions, boundary conditions, and physical parameters. Recent advances in scalable neural operators (McCabe et al., 2024; Cao et al., 2025; Ye et al., 2025a; Zhou et al., 2025) have demonstrated that large, pre-trained models can capture multiple physical systems within a single

<sup>1</sup>MIT MechE <sup>2</sup>MIT CSAIL. Correspondence to: Zituo Chen <zituo@mit.edu>.

architecture, motivating the vision of PDE foundation models. Despite strong short-horizon accuracy, most existing approaches rely on deterministic mappings from current to future states. When deployed autoregressively, these models suffer from compounding error accumulation due to model-inference mismatch and distribution shift, as prediction errors are recursively fed back into subsequent steps (Lippe et al., 2023; Ye et al., 2025b).

Stochastic generative models provide an alternative paradigm by producing ensembles of future states rather than single deterministic trajectories. Such capability is essential for applications that require uncertainty quantification and probabilistic forecasting, including weather prediction (Price et al., 2024; Li et al., 2024a; Hatanpää et al., 2025), data assimilation (Bao et al., 2024b;a), and reliability-based design (Chen et al., 2022; Jiang et al., 2025). Beyond ensemble prediction, stochasticity offers a potential mechanism for stabilizing long-term rollouts by allowing trajectories to re-enter the data manifold instead of drifting irreversibly due to small modeling errors.

In this work, we argue that stable and generalizable neural PDE solvers require *both* a unified latent physics representation and an uncertainty-aware temporal evolution mechanism. To this end, we introduce a latent physics space in which high-dimensional PDE states  $\mathbf{X}$  are mapped to compact representations  $\mathbf{x}$  that preserve essential dynamical structure while abstracting away discretization- and resolution-specific details. Learning dynamics in this space decouples spatial representation learning from temporal modeling, enabling efficient training and inference and facilitating zero-shot generalization across datasets with varying resolutions and geometries. Building upon this latent representation, we propose a probabilistic neural PDE solver that explicitly models uncertainty arising from imperfect state estimates and ambiguous dynamics inference. Our solver employs on-manifold flow forcing to identify latent physical dynamics and uses flow matching to transport states across time in a generative manner. By perturbing latent states with isotropic Gaussian noise, the model learns to denoise perturbed trajectories and return them to physically consistent manifolds, yielding an auto-correcting mechanism that stabilizes long-term rollouts.

Motivated by empirical scaling laws observed in large lan-

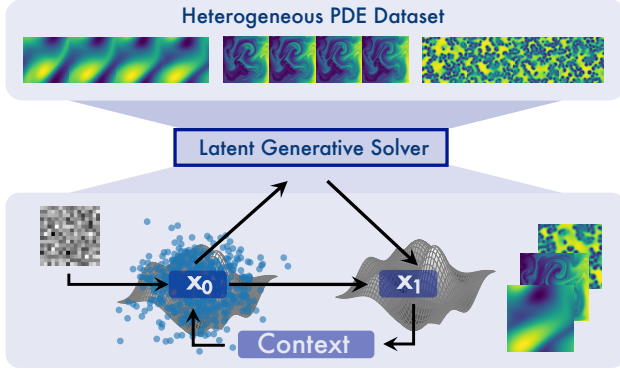


Figure 1. Overview of Latent Generative Solver. All physics states are leveraged into a unified latent space, where initial condition  $x_0$  are perturbed with noise to cover off-manifold self-rollout states, which are guided back to clean next state  $x_1$ . The predicted states serve to generating system dynamics descriptor ‘‘context’’ which differentiate heterogeneous physical dynamics.

guage models (Kaplan et al., 2020; Hoffmann et al., 2022), we further investigate whether similar benefits arise from increasing data diversity in neural PDE solvers. We aggregate heterogeneous public PDE datasets, including FNO-v (Li et al., 2021), PDEArena (Gupta & Brandstetter, 2022), PDEBench (Takamoto et al., 2024), and The Well (Ohana et al., 2025), forming a corpus of 2.5 million trajectories of length five, unified at a spatial resolution of  $128^2$  across 12 distinct PDE families. This dataset enables systematic evaluation of long-term stability, uncertainty propagation, and cross-dynamics generalization under a unified training protocol. The curated dataset further motivates benchmarking representative deterministic baselines, including U-AFNO (Bonneville et al., 2025), CNextU-Net (Ibtehaz & Kihara, 2023), and DPOT (Hao et al., 2024). By standardizing training schedules and learning targets, our benchmarks provide a fair comparison framework for future research on neural PDE solvers.

## Contributions.

- We introduce a latent physics representation that enables resolution-invariant, cross-dynamics generalization while substantially reducing computational cost.
- We propose an uncertainty-aware generative PDE solver based on flow matching with diffusion forcing that yields stable and auto-correcting long-term predictions.
- We curate a large-scale, multi-dynamics PDE dataset and establish unified benchmarks for evaluating deterministic and generative neural PDE solvers.

## 2. Related Work

We review prior work on neural PDE solvers and probabilistic generative approaches for PDE modeling, situating our method within the broader literature.

**Neural PDE solvers.** Neural operators are data-driven surrogate models designed to approximate solution operators of PDEs. Representative methods include Fourier Neural Operators (FNO) (Li et al., 2021), DeepONet (Lu et al., 2021), Physics-Informed Neural Operators ( PINO) (Li et al., 2024b), OFormer (Li et al., 2023), and UPT (Alkin et al., 2024). These models achieve fast inference and exhibit partial generalization to unseen input fields (Kovachki et al., 2023; Azizzadenesheli et al., 2024; Kramer et al., 2024). Transformer-based neural operators, such as ICON (Yang et al., 2023; Cao et al., 2025), MPP (McCabe et al., 2024), DPOT (Hao et al., 2024), PROSE (Liu et al., 2024; Sun et al., 2025), PITT (Lorsung et al., 2024), and PI-MFM (Zhu et al., 2025), leverage large-scale pretraining to model multiple physical dynamics within a unified architecture and often demonstrate favorable scaling behavior. Despite these advances, most neural operators remain deterministic and struggle with long-term autoregressive stability.

**Probabilistic neural PDE solvers.** Probabilistic generative models, including diffusion (Sohl-Dickstein et al., 2015; Ho et al., 2020; Song et al., 2021) and flow matching methods (Lipman et al., 2023; Liu et al., 2022), have been applied to PDE-related tasks to improve uncertainty modeling and sample quality. DiffusionPDE (Huang et al., 2024), CoNFiLD (Du et al., 2024), FunDPS (Yao et al., 2025), and FunDiff (Wang et al., 2025) primarily address inverse problems or state reconstruction under sparse and noisy observations. Other works, including PDERefiner (Lippe et al., 2023), WDNO (Hu et al., 2025), FluidZero (Feng et al., 2025), and DiffusionNO (Oommen et al., 2025), model spatiotemporal dynamics via conditional generative sampling.

While these approaches demonstrate improved accuracy and physical consistency, they are typically limited to single PDE dynamics and short horizons. History-conditioned, long-term generative solvers that generalize across heterogeneous dynamics remain largely unexplored.

**Diffusion forcing for long-term stability.** Autoregressive generation is known to suffer from exposure bias, where errors accumulate as generated outputs are reused as inputs (Arora et al., 2023). Diffusion forcing (Chen et al., 2024) mitigates this issue by generating future states conditioned on partially denoised histories. Subsequent works extend this idea to improve generation quality and efficiency in video modeling (Xie et al., 2025; Zhou et al., 2024; Gao et al., 2024; 2025; Huang et al., 2025). Our work adapts diffusion forcing to the context of PDE dynamics in a latent

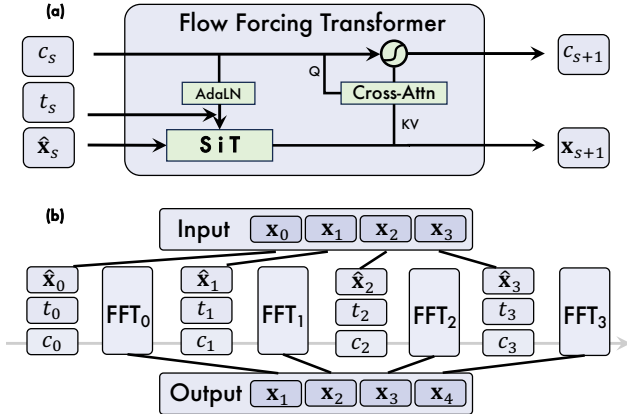


Figure 2. Model Architecture. (a) Essential components of the Flow Forcing Transformer, that first generate next state  $\mathbf{x}_{s+1}$  given intermediate state  $\hat{\mathbf{x}}_s$ , diffusion time  $t_s$ , and physics context  $c_s$ . Then leveraging the generated state, a gated cross-attention unit that updates the physics condition to be  $c_{s+1}$ . (b) A set of FFTs to realize the next-state-prediction during training, where intermediate states are transformed from inputs and sequential FFTs autoregressively inherit context  $c$  and make prediction at each step.

physics space, enabling uncertainty-aware, stable long-term prediction across multiple physical systems.

### 3. Method

We study multi-dynamics autoregressive one-step prediction with a fixed-length history window

$$p(\mathbf{X}_{s+1} \mid \mathbf{X}_{0:s}), \quad s = 0, 1, 2, \dots, \quad (1)$$

where  $\mathbf{X}_s \in \mathcal{X} \subset \mathbb{R}^{H \times W \times C}$  denotes the physical state at physical time  $s$ . We will also use an auxiliary transport time  $t \in [0, 1]$  within each physical transition  $s \rightarrow s + 1$  for flow-based generation;  $t$  should not be confused with the PDE time index  $s$ .

#### 3.1. Learning Latent Physics

We introduce a unified latent physics representation that coordinates heterogeneous PDE systems while improving generalization and computational efficiency.

A Pretrained-Physics Variational Autoencoder (P2VAE) maps high-dimensional physical states  $\mathbf{X}$  into a shared latent space  $\mathbf{x}$ . All dynamics prediction is performed in latent space, while the decoder is used only for reconstruction and evaluation. P2VAE is trained independently of downstream solvers and reused across tasks and system instances. The latent space captures system-invariant dynamical structure while discarding representation-specific redundancy such as resolution and discretization artifacts, enabling different PDE systems with similar dynamics to occupy nearby latent regions and improving cross-dataset generalization.

Decoupling representation learning from temporal modeling allows the encoder to absorb geometric variability and multi-scale spatial correlations, while the dynamics model focuses on temporal evolution and uncertainty propagation in latent space. This modular design simplifies optimization and supports reuse of the latent representation across different predictors and objectives.

Latent states are also significantly lower-dimensional than the original fields, reducing memory footprint and accelerating both training and inference. Latent trajectories can be precomputed and cached, eliminating repeated encoding during solver training and making long-horizon autoregressive learning more efficient.

Finally, the compact and continuous latent space provides a natural substrate for probabilistic modeling, allowing uncertainty to be injected and propagated in a controlled and physically meaningful manner compared to perturbations applied directly in the original state space.

#### 3.2. Uncertainty-Aware Generative Solver

With the unified physics space, we next introduce an uncertainty-aware generative dynamics solver that explicitly accounts for both state uncertainty and latent dynamics ambiguity over long-term rollouts.

Inspired by equation-driven conditioning in neural operators, we introduce a latent dynamics variable  $c_s$  inferred from history and factorize

$$p(\mathbf{x}_{s+1} \mid \mathbf{x}_{0:s}) = \int p(\mathbf{x}_{s+1} \mid \mathbf{x}_s, c_s) p(c_s \mid \mathbf{x}_{0:s-1}) dc_s \quad (2)$$

Here  $c_s$  captures underlying dynamics inferred from history. This factorization exposes two stability bottlenecks: (i) state uncertainty in  $\mathbf{x}_s$  because it is model-generated at test time and may drift off the data manifold; (ii) dynamics uncertainty in  $c_s$  due to finite observations and model ambiguity. We address (i) by a flow-matching transition equipped with an uncertainty knob, and (ii) by a flow-forcing scheme that updates  $c_s$  on the model manifold. Together they form our dynamics predictor Flow Forcing Transformer (FFT).

**Flow matching with an uncertainty knob.** We model  $p(\mathbf{x}_{s+1} \mid \mathbf{x}_s, c_s)$  via a conditional probability flow. For clarity we suppress  $s$  and write  $(\mathbf{x}_0, \mathbf{x}_1)$  for consecutive latent states. At test time, the input  $\mathbf{x}_0$  is perturbed by rollout error; thus we train the model on a softened source distribution. Define the  $k$ -softened source random variable

$$\tilde{\mathbf{x}}_0^k := (1 - k)\mathbf{x}_0 + k\mathbf{z}, \quad \mathbf{z} \sim \mathcal{N}(0, \mathbf{I}), \quad k \in [0, 1], \quad (3)$$

which induces a distribution  $\tilde{\pi}_0^k$  over  $\tilde{\mathbf{x}}_0^k$ . The scalar  $k$  controls the magnitude of off-manifold perturbations and serves as an *uncertainty knob* during both training and inference.

We construct intermediate bridge states by linear interpolation between softened source and target:

$$\mathbf{x}_t^k := (1-t)\tilde{\mathbf{x}}_0^k + t\mathbf{x}_1, \quad t \sim \mathcal{U}(0, 1). \quad (4)$$

Conditioned on  $(\tilde{\mathbf{x}}_0^k, \mathbf{x}_1)$ , the sample-wise velocity along this path admits the identity

$$\mathbf{u}_t^k := \frac{d}{dt}\mathbf{x}_t^k = \mathbf{x}_1 - \tilde{\mathbf{x}}_0^k = \frac{\mathbf{x}_1 - \mathbf{x}_t^k}{1-t}. \quad (5)$$

Inspired by JiT (Li & He, 2026), we parameterize the model to predict the endpoint ( $\mathbf{x}$ -pred) and minimize v-loss objective:

$$\hat{\mathbf{x}}_1 = \mathbf{g}_\theta(\mathbf{x}_t^k, t, c), \quad (6)$$

$$\mathbf{v}_\theta := \frac{\hat{\mathbf{x}}_1 - \mathbf{x}_t^k}{1-t}. \quad (7)$$

$$\mathcal{L}_{\text{FM}} = \mathbb{E} \left[ \|\mathbf{v}_\theta - \mathbf{u}_t^k\|_2^2 \right] = \mathbb{E} \left[ \left\| \frac{\hat{\mathbf{x}}_1 - \mathbf{x}_t^k}{1-t} \right\|_2^2 \right], \quad (8)$$

where the last equality follows by substituting (5) and (7). We clamp  $(1-t) \geq \tau$  for numerical stability ( $\tau = 0.05$ ).

At inference, we integrate the probability-flow ODE

$$\frac{d\mathbf{x}}{dt} = \mathbf{v}_\theta(\mathbf{x}, t, c), \quad \mathbf{x}(0) = \tilde{\mathbf{x}}_0^k, \quad (9)$$

from  $t = 0$  to  $t = 1 - \epsilon$ , and take the model output at last timestep as the predicted next state.

Training with  $k > 0$  exposes the model to off-manifold inputs  $\tilde{\mathbf{x}}_0^k$  that mimic rollout errors, and forces the learned flow to transport a neighborhood of the data manifold toward plausible next states. At inference, sampling  $\mathbf{z}$  and choosing  $k$  produces an ensemble of corrective transitions, enabling stable long-horizon rollouts via re-entry to the learned manifold.

**Flow forcing on the data manifold.** Conceptually, the physical context evolves as a filtering process:

$$c_s \sim p(c_s | c_{s-1}, \mathbf{x}_s). \quad (10)$$

At test time, this update should depend on model-generated  $\hat{\mathbf{x}}_s$ , whereas naive training would update  $c_s$  using ground-truth states, creating exposure bias. Concretely, at physical step  $s$ , after predicting  $\hat{\mathbf{x}}_{s+1}$  conditioned on  $c_s$ , we update  $c_{s+1}$  using a gated cross-attention interaction between  $\hat{\mathbf{x}}_{s+1}$  and  $c_s$  (Figure 2a),

$$c_{s+1} = \text{Gate}(c_s, \text{Attn}(\hat{\mathbf{x}}_{s+1}, c_s)). \quad (11)$$

Thus, during training, all subsequent conditioning is driven by model-generated trajectories, aligning train and test distributions and empirically stabilizing long-horizon rollouts.

Due to the quadratic complexity of self-attention over long histories, we introduce temporal pyramids to reduce token counts, reflecting the approximate Markovian property of many PDE systems. For early  $s$ , we use downsampled (average-pooled) latent states to propagate the physical context  $c$ ; yielding a Pyramidal FFT (PFFT).

### 3.3. Training and Inference

We adopt a two-stage training protocol.

**Stage I: Latent Physics Encoding.** P2VAE learns a compact latent physics space by reconstructing individual system states while regularizing the latent distribution toward a standard normal prior. After convergence, the encoder is frozen and used to precompute all latent trajectories.

**Stage II: Latent Dynamics Learning.** PFFT is trained on precomputed latent trajectories using sequential flow forcing. For each step, a softened source state is constructed by mixing the current latent with Gaussian noise via a scalar uncertainty knob  $k$ . A random bridge time  $t$  defines an interpolation between the softened source and the next latent state. The model predicts the endpoint, and parameters are optimized using a flow-matching loss. Conditioning variables are updated autoregressively on the learned model manifold. Early latent states are temporally downsampled using a pyramid scheme for acceleration.

**Inference and Rollout.** At inference time, the learned latent solver is rolled out autoregressively. Given an initial latent history, the next latent state is generated by integrating the probability-flow ODE from a noise-perturbed latent input. Predicted latent states are decoded back to physical space using the P2VAE decoder.

### 3.4. Compounding Error: Deterministic Operators vs. Flow Matching

We analyze how rollout errors propagate under deterministic autoregressive operators and contrast this with probability-flow transitions trained using the  $k$ -softened flow-matching objective in Equation (8).

**Deterministic autoregressive operators.** Let  $\Phi : \mathcal{X} \rightarrow \mathcal{X}$  denote the true one-step latent dynamics and let  $f_\theta : \mathcal{X} \rightarrow \mathcal{X}$  be a deterministic learned operator trained by one-step regression. The true and predicted rollouts satisfy

$$\mathbf{x}_{n+1}^* = \Phi(\mathbf{x}_n^*), \quad \mathbf{x}_{n+1} = f_\theta(\mathbf{x}_n), \quad (12)$$

and we define the rollout error  $\delta_n := \mathbf{x}_n - \mathbf{x}_n^*$  and the one-step model error  $e_n := f_\theta(\mathbf{x}_n) - \Phi(\mathbf{x}_n)$ .

**Assumption 3.1** (Lipschitz true dynamics).  $\Phi$  is  $L$ -Lipschitz:  $\|\Phi(\mathbf{x}) - \Phi(\mathbf{y})\| \leq L\|\mathbf{x} - \mathbf{y}\|$ .

**Proposition 3.2** (Deterministic compounding error). *Under Assumption 3.1,*

$$\|\delta_{n+1}\| \leq \|e_n\| + L\|\delta_n\|. \quad (13)$$

If  $\delta_0 = 0$ , then

$$\|\delta_n\| \leq \sum_{j=0}^{n-1} L^{n-1-j} \|e_j\|. \quad (14)$$

When  $L > 1$ , rollout error grows geometrically even if the one-step regression error is small. This instability is intrinsic to deterministic autoregressive prediction models and is not mitigated by the training objective.

**Probability-flow transitions with a softened source.** In contrast, flow matching does not iterate a deterministic map. At each step, the input state  $\mathbf{x}_0$  is first perturbed via the  $k$ -softened source (3), and the next state is generated by integrating the PF-ODE (9) starting from  $\tilde{\mathbf{x}}_0^k$ .

Let  $\mathbf{v}^*(\mathbf{x}, t, c)$  denote the reference velocity field corresponding to the true conditional transition and write

$$\mathbf{v}_\theta(\mathbf{x}, t, c) = \mathbf{v}^*(\mathbf{x}, t, c) + \mathbf{r}(\mathbf{x}, t, c),$$

where  $\mathbf{r}$  is the learned residual induced by minimizing the flow-matching loss (8).

**Assumption 3.3** (Residual regularity). For fixed  $c$ , the scaled residual  $(1-t)\mathbf{r}(\cdot, t, c)$  is Lipschitz continuous in  $\mathbf{x}$  with constant  $L_r(t)$ :

$$\|(1-t)(\mathbf{r}(\mathbf{x}, t, c) - \mathbf{r}(\mathbf{y}, t, c))\| \leq L_r(t)\|\mathbf{x} - \mathbf{y}\|.$$

**Theorem 3.4** (One-step probability-flow deviation). *Fix  $c$  and  $k$ . Let  $\mathbf{x}(t)$  and  $\mathbf{x}^*(t)$  be solutions of the PF-ODE (9) driven by  $\mathbf{v}_\theta$  and  $\mathbf{v}^*$  respectively, with identical initial condition  $\mathbf{x}(0) = \tilde{\mathbf{x}}_0^k$ . Under Assumption 3.3, for any  $\epsilon \in (0, 1)$ ,*

$$\|\mathbf{x}(1-\epsilon) - \mathbf{x}^*(1-\epsilon)\| \leq \epsilon \exp\left(\int_0^{1-\epsilon} \frac{L_r(t)}{1-t} dt\right) \int_0^{1-\epsilon} \frac{\|\boldsymbol{\eta}(t)\|}{\epsilon(1-t)} dt, \quad (15)$$

where  $\boldsymbol{\eta}(t) := (1-t)\mathbf{r}(\mathbf{x}^*(t), t, c)$ .

The bound depends on the learned residual  $\mathbf{r}$  along the probability-flow path and does not involve the global Lipschitz constant of the one-step map  $\Phi$ .

**Multi-step rollout behavior.** Autoregressive flow-matching rollouts alternate between stochastic re-anchoring and probability-flow transport. Let  $\delta_s$  denote the deviation between the predicted and reference latent states before

softening at step  $s$ . Form  $\tilde{\mathbf{x}}_s^k$  and  $\tilde{\mathbf{x}}_s^{*,k}$  using the same noise realization  $\mathbf{z}$ . Then

$$\tilde{\delta}_s := \tilde{\mathbf{x}}_s^k - \tilde{\mathbf{x}}_s^{*,k} = (1-k)\delta_s.$$

The subsequent PF-ODE integration contributes an additional deviation controlled by Theorem 3.4. Consequently, the expected rollout error satisfies a damped recursion

$$\mathbb{E}\|\delta_{s+1}\| \leq (1-k)\mathbb{E}\|\delta_s\| + C \sup_{t \in [0,1]} \|\boldsymbol{\eta}(t)\|, \quad (16)$$

where  $C$  is the constant induced by the exponential factor in Theorem 3.4.

**Comparison.** Deterministic operators propagate error through repeated application of a fixed map and inherit the global Lipschitz constant of the true dynamics, leading to compounding error. Flow matching instead controls error locally at each step through residual learning and suppresses accumulation via stochastic re-entry to the learned manifold. As a result, stable long-horizon rollouts are achieved without requiring contractive physical dynamics.

## 4. Experiment Setup

### 4.1. General setup

**Dataset gathering.** We consider a combination of public PDE simulation benchmark datasets FNO-v, PDEBench, PDEArena, and the Well to form a heterogeneous dataset. All the dynamical systems are 2D intrinsically. We compressed the aforementioned datasets to the format of  $128^2$  resolution with 3 multiphysics channels (c3p128) with float16 precision to form a 233 GB dataset. We provide the exact compression ratio and detailed dataset information in Appendix B.

**Implementation details.** P2VAE shares the standard SD-VAE (Rombach et al., 2022) architecture to compress each state from c3p128 to c16p16 ( $12 \times$  compression rate). PFPT is implemented with modern architectures RMSNorm, SwiGLU, and FlashAttention v2 (Dao, 2023) in the Transformer module. P2VAE (249M) is trained for 100k steps with KL term's weight  $\beta = 1e-6$ . Latent states are computed after the P2VAE convergence, and stored for PFPT training. PFPT (138M) is trained on the latent states dataset for another 100k steps. More details should be found in Appendix C.1.

**Evaluation.** We employ L2 relative error (L2RE) as the evaluation metric, despite mean squared error (MSE) is the training objective. As a summarizing score, we use the averaged L2RE of 1-step prediction among 16 systems to represent each model's general capability.

## 4.2. Baselines

Baseline methods include: U-AFNO, CNextU-Net and DPOT, respectively the advanced models of FNO-based, U-net-based and Transformer-based neural operators. For all benchmarks, we implemented our version of the code due to misalignment across previous works, such as training schedules and context lengths. In our case, all models are set up with a context length of 4 as concatenated input, and trained for 200k steps given an identical optimizer configuration. Implementation details should be found in Appendix C.2

## 4.3. Ablation Studies

We design ablations to isolate which components of PFPT are responsible for (i) long-horizon rollout stability and (ii) efficiency. All models operate in the same latent space (same frozen P2VAE) and use the same context length (4) unless noted. We report Avg. L2RE for 1/5/10-step rollouts and FLOPs.

Our full objective is the factorized latent transition  $p(\mathbf{x}_{s+1} \mid \mathbf{x}_{0:s}) = \int p(\mathbf{x}_{s+1} \mid \mathbf{x}_s, c_s) p(c_s \mid \mathbf{x}_{0:s-1}) dc_s$  with (a) generative modeling of  $p(\mathbf{x}_{s+1} \mid \mathbf{x}_s, c_s)$ , (b) flow forcing coverage where each  $\mathbf{x}_{1:s+1}$  gets supervised, (c) uncertainty knob  $k$  (Eq. (3)), (d) maintenance of physical context  $c_{s+1} = \text{Update}(c_s, \hat{\mathbf{x}}_{s+1})$  (Eq. (11)), and (e) temporal pyramids for efficient history conditioning. The ablation models ablates from (e) to (a) by order of A1-A4. Implementation details are provided in Appendix C.3.

## 5. Experiment Results

Sampled trajectories generated by LGS on the test sets of all 15 PDE systems are provided in Appendix D. We highlight three case studies that illustrate the capabilities of Latent Generative Solver.

### 5.1. Dynamics Condition Clustering

LGS infers a system-specific physics context  $c$  through the context inference process. Figure 3 visualizes sampled contexts using t-SNE. We observe two properties: (i) contexts are nearly invariant across the diffusion/transport process, consistent with context updates being driven by model-predicted next states on the learned manifold (Equation (11)); (ii) contexts cluster by system identity and remain separated despite differences in spatial patterns. These results suggest that the learned context can serve as a compact descriptor of system dynamics, which may enable future equation-driven or multi-modal conditioning.

## 5.2. Long-term Rollout Stability

We first compare 1-step prediction accuracy of LGS with deterministic baselines in Table 1. LGS is comparable to strong baselines such as U-AFNO and DPOT at 1 step. We then evaluate 5-step and 10-step rollouts to assess long-horizon stability, and include all ablation variants. Figure 4a reports the average L2RE over 16 systems versus training throughput measured on an H200 GPU with batch size 64. Marker area indicates per-sample forward FLOPs. Figure 4b shows a representative rollout from FNO-v3, where LGS maintains coherent structure while the deterministic baseline accumulates artifacts over time.

A1 achieves the best accuracy, but its throughput is comparable to DPOT. One likely reason is the forcing schedule: during training, LGS produces four supervised predictions per physical step, whereas deterministic baselines predict only the next state once. With temporal pyramids, LGS recovers most of A1’s accuracy while reducing the attention cost of conditioning on full-resolution history.

### 5.3. Generalization on OOD High-Res Dynamics

Although both U-AFNO and LGS accept variable-resolution inputs, they differ in adaptation efficiency. We report out-of-distribution performance on a  $256^2$  2D Kolmogorov flow dataset for 1-step, 5-step, and 10-step rollouts as a function of adaptation budget (Table 2). Our goal is not extreme few-shot learning, but measuring adaptation under a constrained budget: 10% of the target training data for 5 epochs.

Both models produce reasonable short-horizon predictions at initialization, but LGS adapts substantially faster than U-AFNO (Table 2). Under self-rollout, U-AFNO exhibits blurred structures and compounding drift typical of deterministic mappings. In contrast, LGS produces a more stable, damped evolution of the Kolmogorov flow and improves consistently with finetuning (Figure 5).

## 6. Conclusion

In this paper, we propose Latent Generative Solver, which predicts future system states from a sequence of past states in latent space. While deterministic baselines suffer from compounding errors during long-horizon autoregressive rollouts, the proposed uncertainty-aware design enables more stable prediction. The model also demonstrates the ability to represent diverse physical dynamics through large-scale pretraining, and generalizes effectively to unseen spatial resolutions and out-of-distribution physical systems.

We envision this generative framework as a foundational tool for PDE-related research with real-world impact. On the architectural side, further advances in Transformer models may enable more expressive and accurate dynamics mod-

Table 1. Benchmarks of baseline methods compared to P2VAE as the upper bound for learning in latent space and our model LGS. Models are kept in similar parameter size  $\sim 150M$ . The unit is L2RE in percentage.

MODEL	FNO-v5	FNO-v4	FNO-v3	PA-NS	PA-NSC	PA-SWE	PB-CNSL	PB-CNSH
CNEXTU-NET-153M	6.18	28.3	2.64	29.5	21.4	10.5	73.6	73.0
DPOT-160M	3.78	<b>8.00</b>	1.39	20.9	5.61	9.50	<b>1.32</b>	4.48
U-AFNO-152M	<b>3.45</b>	8.40	1.39	<b>16.4</b>	5.13	<b>6.67</b>	1.33	<b>4.28</b>
LGS-249+138M	4.74	8.77	<b>1.22</b>	16.6	<b>4.35</b>	8.18	1.60	4.90
P2VAE-249M <sup>†</sup>	2.49	1.26	0.77	6.18	3.78	6.52	0.49	1.22

MODEL	PB-SWE	W-AM	W-GS	W-SWE	W-RB	W-SF	W-TR	W-VE
CNEXTU-NET-153M	7.85	12.3	5.51	15.1	10.7	7.68	8.17	20.9
DPOT-160M	5.39	<b>4.40</b>	3.83	3.01	9.19	7.49	6.36	3.71
U-AFNO-152M	<b>2.90</b>	4.63	<b>3.28</b>	<b>1.29</b>	7.75	<b>3.89</b>	6.39	<b>3.55</b>
LGS-249+138M	6.42	4.41	3.80	4.91	<b>6.73</b>	9.67	<b>4.95</b>	4.15
P2VAE-249M <sup>†</sup>	5.39	1.21	1.67	3.27	6.46	6.45	2.11	1.88

<sup>†</sup> P2VAE is a latent representation model and does not perform end-to-end rollout prediction; results are not directly comparable.

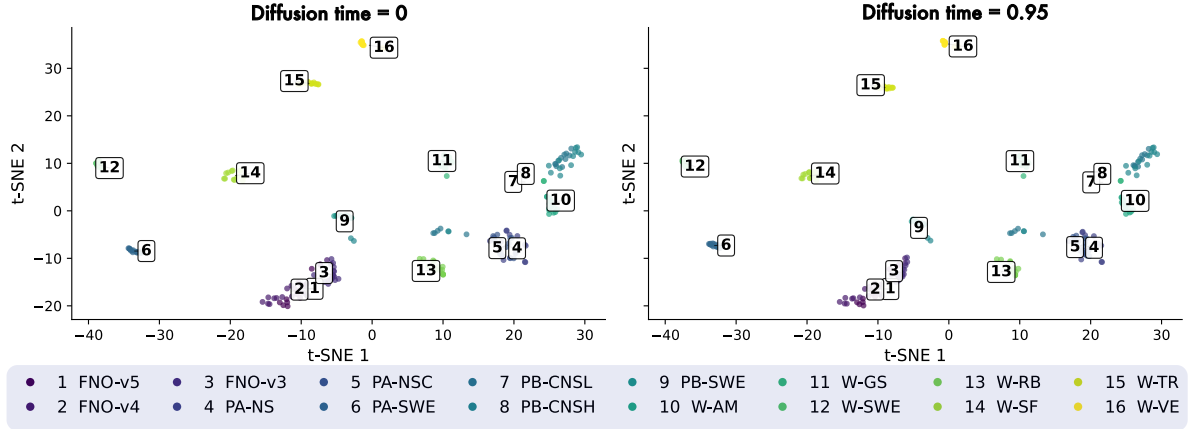


Figure 3. t-SNE visualization of inferred physics contexts  $c$  for different PDE systems at the beginning and end of prediction. Each system forms a stable cluster and exhibits minimal drift over the diffusion/transport steps, indicating that context updates remain on the learned manifold.

Table 2. 1-step L2RE during finetuning on  $256^2$  Kolmogorov flow (lower is better).

Model	Zero-shot	Epoch 2	Epoch 5
U-AFNO	0.6528	0.5789	0.3430
LGS	0.3984	0.1781	0.1291

eling, while autoencoders defined in functional spaces may alleviate current reconstruction bottlenecks. Beyond surrogate simulation, the proposed solver naturally extends to downstream applications such as digital twins for active control and data assimilation with sparse observations, where long-term stability and uncertainty awareness are essential for reliable deployment.

## Impact Statement

This work advances machine-learning methods for scientific computing by improving the reliability and efficiency of learned PDE surrogates. By modeling uncertainty and mitigating long-horizon rollout drift, our approach can support ensemble forecasting, rapid parameter sweeps, and accelerated experimentation loops in domains such as fluids, climate-relevant geophysical flows, and multiphysics simulation. Potential positive impacts include reduced computational cost and energy consumption relative to repeatedly running high-fidelity solvers, and improved uncertainty-aware decision-making when surrogate predictions are used in downstream tasks (e.g., design optimization or data assimilation). Potential risks arise if fast surrogates are deployed outside their validity regime or interpreted as ground truth; this is particularly relevant in safety-critical settings. We therefore emphasize evaluation on out-of-distribution dynamics/resolutions, reporting of uncertainty and failure

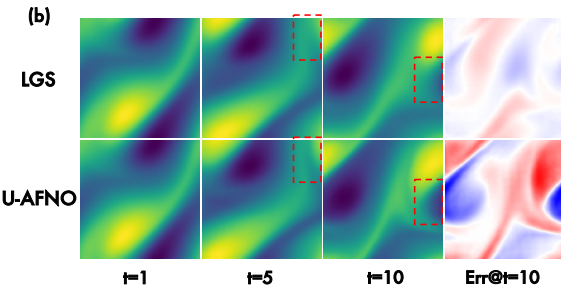
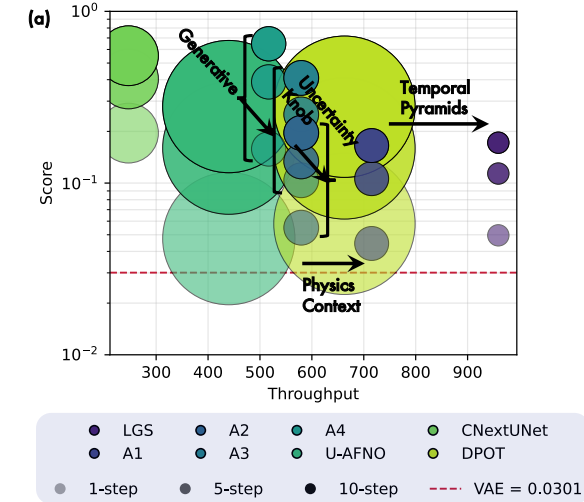


Figure 4. (a) Average L2RE over 16 systems versus training throughput. Marker area denotes per-sample forward FLOPs. Latent-space models (LGS and ablations) have substantially lower FLOPs. Physics context and temporal pyramids improve throughput with limited loss of accuracy, while generative modeling and the uncertainty knob improve rollout accuracy. (b) Example 10-step rollout on FNO-v3 comparing LGS and U-AFNO. Errors accumulate and amplify into visible artifacts for the deterministic baseline (highlighted region). Error is visualized with a fixed range of  $(-0.5, 0.5)$ .

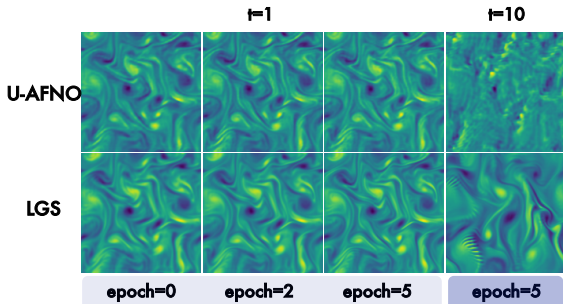


Figure 5. OOD adaptation on  $256^2$  Kolmogorov flow. Left: 1-step predictions after finetuning. Right: 10-step autoregressive rollouts of the finetuned models. LGS better preserves coherent vorticity structures and exhibits reduced long-horizon drift.

cases, and the continued use of physical solvers or measurements for verification when high-stakes decisions are involved.

## References

Alkin, B., Fürst, A., Schmid, S., Gruber, L., Holzleitner, M., and Brandstetter, J. Universal physics transformers: A framework for efficiently scaling neural operators. *Advances in Neural Information Processing Systems*, 37: 25152–25194, 2024.

Arora, K., Asri, L. E., Bahuleyan, H., and Cheung, J. C. K. Why exposure bias matters: An imitation learning perspective of error accumulation in language generation, 2023. URL <https://arxiv.org/abs/2204.01171>.

Azizzadenesheli, K., Kovachki, N., Li, Z., Liu-Schiavini, M., Kossaifi, J., and Anandkumar, A. Neural operators for accelerating scientific simulations and design. *Nature Reviews Physics*, 6(5):320–328, 2024.

Bao, F., Chipilski, H. G., Liang, S., Zhang, G., and Whitaker, J. S. Nonlinear ensemble filtering with diffusion models: Application to the surface quasi-geostrophic dynamics, 2024a. URL <https://arxiv.org/abs/2404.00844>.

Bao, F., Zhang, Z., and Zhang, G. A score-based filter for nonlinear data assimilation. *Journal of Computational Physics*, 514:113207, 2024b.

Bonneville, C., Bieberdorf, N., Hegde, A., Asta, M., Najm, H. N., Capolungo, L., and Safta, C. Accelerating phase field simulations through a hybrid adaptive fourier neural operator with u-net backbone. *npj Computational Materials*, 11(1), January 2025. ISSN 2057-3960. doi: 10.1038/s41524-024-01488-z. URL <http://dx.doi.org/10.1038/s41524-024-01488-z>.

Cao, Y., Liu, Y., Yang, L., Yu, R., Schaeffer, H., and Osher, S. Vicon: Vision in-context operator networks for multi-physics fluid dynamics prediction, 2025. URL <https://arxiv.org/abs/2411.16063>.

Chen, B., Monso, D. M., Du, Y., Simchowitz, M., Tedrake, R., and Sitzmann, V. Diffusion forcing: Next-token prediction meets full-sequence diffusion, 2024. URL <https://arxiv.org/abs/2407.01392>.

Chen, W. W., Lee, D., Balogun, O., and Chen, W. Gan-duf: Hierarchical deep generative models for design under free-form geometric uncertainty, 2022. URL <https://arxiv.org/abs/2202.10558>.

Dao, T. Flashattention-2: Faster attention with better parallelism and work partitioning, 2023. URL <https://arxiv.org/abs/2307.08691>.

Du, P., Parikh, M. H., Fan, X., Liu, X.-Y., and Wang, J.-X. Conditional neural field latent diffusion model for generating spatiotemporal turbulence. *Nature Communications*, 15(1):10416, 2024.

Feng, H., Zheng, H., Hu, P., Liu, H., Yu, C., Wei, L., Feng, R., Duan, J., Fan, D., and Wu, T. Fluidzero: Mastering diverse tasks in fluid systems through a single generative model. 2025.

Gao, J., Cao, Q., and Chen, Y. Auto-regressive moving diffusion models for time series forecasting, 2024. URL <https://arxiv.org/abs/2412.09328>.

Gao, K., Shi, J., Zhang, H., Wang, C., Xiao, J., and Chen, L. Ca2-vdm: Efficient autoregressive video diffusion model with causal generation and cache sharing, 2025. URL <https://arxiv.org/abs/2411.16375>.

Gupta, J. K. and Brandstetter, J. Towards multi-spatiotemporal-scale generalized pde modeling, 2022. URL <https://arxiv.org/abs/2209.15616>.

Hao, Z., Su, C., Liu, S., Berner, J., Ying, C., Su, H., Anandkumar, A., Song, J., and Zhu, J. Dpot: Auto-regressive denoising operator transformer for large-scale pde pre-training, 2024. URL <https://arxiv.org/abs/2403.03542>.

Hatanpää, V., Ku, E., Stock, J., Emani, M., Foreman, S., Jung, C., Madireddy, S., Nguyen, T., Sastry, V., Sinurat, R. A. O., Wheeler, S., Zheng, H., Arcomano, T., Vishwanath, V., and Kotamarthi, R. Aeris: Argonne earth systems model for reliable and skillful predictions, 2025. URL <https://arxiv.org/abs/2509.13523>.

Ho, J., Jain, A., and Abbeel, P. Denoising diffusion probabilistic models, 2020. URL <https://arxiv.org/abs/2006.11239>.

Hoffmann, J., Borgeaud, S., Mensch, A., Buchatskaya, E., Cai, T., Rutherford, E., de Las Casas, D., Hendricks, L. A., Welbl, J., Clark, A., Hennigan, T., Noland, E., Millican, K., van den Driessche, G., Damoc, B., Guy, A., Osindero, S., Simonyan, K., Elsen, E., Rae, J. W., Vinyals, O., and Sifre, L. Training compute-optimal large language models, 2022. URL <https://arxiv.org/abs/2203.15556>.

Hu, P., Wang, R., Zheng, X., Zhang, T., Feng, H., Feng, R., Wei, L., Wang, Y., Ma, Z.-M., and Wu, T. Wavelet diffusion neural operator, 2025. URL <https://arxiv.org/abs/2412.04833>.

Huang, J., Yang, G., Wang, Z., and Park, J. J. Diffusionpde: Generative pde-solving under partial observation, 2024. URL <https://arxiv.org/abs/2406.17763>.

Huang, X., Li, Z., He, G., Zhou, M., and Shechtman, E. Self forcing: Bridging the train-test gap in autoregressive video diffusion, 2025. URL <https://arxiv.org/abs/2506.08009>.

Ibtehaz, N. and Kihara, D. Acc-unet: A completely convolutional unet model for the 2020s, 2023. URL <https://arxiv.org/abs/2308.13680>.

Jaegle, A., Gimeno, F., Brock, A., Zisserman, A., Vinyals, O., and Carreira, J. Perceiver: General perception with iterative attention, 2021. URL <https://arxiv.org/abs/2103.03206>.

Jiang, Z., Tang, Q., and Wang, Z. Generative reliability-based design optimization using in-context learning capabilities of large language models, 2025. URL <https://arxiv.org/abs/2503.22401>.

Kaplan, J., McCandlish, S., Henighan, T., Brown, T. B., Chess, B., Child, R., Gray, S., Radford, A., Wu, J., and Amodei, D. Scaling laws for neural language models, 2020. URL <https://arxiv.org/abs/2001.08361>.

Kovachki, N., Li, Z., Liu, B., Azizzadenesheli, K., Bhattacharya, K., Stuart, A., and Anandkumar, A. Neural operator: Learning maps between function spaces with applications to pdes. *Journal of Machine Learning Research*, 24(89):1–97, 2023.

Kramer, B., Peherstorfer, B., and Willcox, K. E. Learning nonlinear reduced models from data with operator inference. *Annual Review of Fluid Mechanics*, 56(1):521–548, 2024.

Li, L., Carver, R., Lopez-Gomez, I., Sha, F., and Anderson, J. Generative emulation of weather forecast ensembles with diffusion models. *Science Advances*, 10(13):eadk4489, 2024a. doi: 10.1126/sciadv.adk4489. URL <https://www.science.org/doi/abs/10.1126/sciadv.adk4489>.

Li, T. and He, K. Back to basics: Let denoising generative models denoise, 2026. URL <https://arxiv.org/abs/2511.13720>.

Li, Z., Kovachki, N., Azizzadenesheli, K., Liu, B., Bhattacharya, K., Stuart, A., and Anandkumar, A. Fourier neural operator for parametric partial differential equations, 2021. URL <https://arxiv.org/abs/2010.08895>.

Li, Z., Meidani, K., and Farimani, A. B. Transformer for partial differential equations' operator learning, 2023. URL <https://arxiv.org/abs/2205.13671>.

Li, Z., Zheng, H., Kovachki, N., Jin, D., Chen, H., Liu, B., Azizzadenesheli, K., and Anandkumar, A. Physics-informed neural operator for learning partial differential equations. *ACM/JMS Journal of Data Science*, 1(3):1–27, 2024b.

Lipman, Y., Chen, R. T. Q., Ben-Hamu, H., Nickel, M., and Le, M. Flow matching for generative modeling, 2023. URL <https://arxiv.org/abs/2210.02747>.

Lippe, P., Veeling, B. S., Perdikaris, P., Turner, R. E., and Brandstetter, J. Pde-refiner: Achieving accurate long rollouts with neural pde solvers, 2023. URL <https://arxiv.org/abs/2308.05732>.

Liu, X., Gong, C., and Liu, Q. Flow straight and fast: Learning to generate and transfer data with rectified flow, 2022. URL <https://arxiv.org/abs/2209.03003>.

Liu, Y., Sun, J., He, X., Pinney, G., Zhang, Z., and Schaeffer, H. Prose-fd: A multimodal pde foundation model for learning multiple operators for forecasting fluid dynamics, 2024. URL <https://arxiv.org/abs/2409.09811>.

Lorsung, C., Li, Z., and Farimani, A. B. Physics informed token transformer for solving partial differential equations. *Machine Learning: Science and Technology*, 5(1):015032, 2024.

Lu, L., Jin, P., Pang, G., Zhang, Z., and Karniadakis, G. E. Learning nonlinear operators via deeponet based on the universal approximation theorem of operators. *Nature machine intelligence*, 3(3):218–229, 2021.

McCabe, M., Blancard, B. R.-S., Parker, L. H., Ohana, R., Cranmer, M., Bietti, A., Eickenberg, M., Golkar, S., Krawezik, G., Lanusse, F., Pettee, M., Tesileanu, T., Cho, K., and Ho, S. Multiple physics pretraining for physical surrogate models, 2024. URL <https://arxiv.org/abs/2310.02994>.

Ohana, R., McCabe, M., Meyer, L., Morel, R., Agocs, F. J., Beneitez, M., Berger, M., Burkhardt, B., Burns, K., Dalziel, S. B., Fielding, D. B., Fortunato, D., Goldberg, J. A., Hirashima, K., Jiang, Y.-F., Kerswell, R. R., Maddu, S., Miller, J., Mukhopadhyay, P., Nixon, S. S., Shen, J., Wateaux, R., Blancard, B. R.-S., Rozet, F., Parker, L. H., Cranmer, M., and Ho, S. The well: a large-scale collection of diverse physics simulations for machine learning, 2025. URL <https://arxiv.org/abs/2412.00568>.

Oommen, V., Bora, A., Zhang, Z., and Karniadakis, G. E. Integrating neural operators with diffusion models improves spectral representation in turbulence modeling, 2025. URL <https://arxiv.org/abs/2409.08477>.

Price, I., Sanchez-Gonzalez, A., Alet, F., Andersson, T. R., El-Kadi, A., Masters, D., Ewalds, T., Stott, J., Mohamed, S., Battaglia, P., Lam, R., and Willson, M. Gencast: Diffusion-based ensemble forecasting for medium-range weather, 2024. URL <https://arxiv.org/abs/2312.15796>.

Rombach, R., Blattmann, A., Lorenz, D., Esser, P., and Ommer, B. High-resolution image synthesis with latent diffusion models, 2022. URL <https://arxiv.org/abs/2112.10752>.

Sohl-Dickstein, J., Weiss, E. A., Maheswaranathan, N., and Ganguli, S. Deep unsupervised learning using nonequilibrium thermodynamics, 2015. URL <https://arxiv.org/abs/1503.03585>.

Song, Y., Durkan, C., Murray, I., and Ermon, S. Maximum likelihood training of score-based diffusion models, 2021. URL <https://arxiv.org/abs/2101.09258>.

Sun, J., Liu, Y., Zhang, Z., and Schaeffer, H. Towards a foundation model for partial differential equations: Multioperator learning and extrapolation. *Physical Review E*, 111(3):035304, 2025.

Takamoto, M., Praditia, T., Leiteritz, R., MacKinlay, D., Alesiani, F., Pflüger, D., and Niepert, M. Pdebench: An extensive benchmark for scientific machine learning, 2024. URL <https://arxiv.org/abs/2210.07182>.

Wang, S., Dou, Z., Shan, S., Liu, T.-R., and Lu, L. Fun-diff: Diffusion models over function spaces for physics-informed generative modeling, 2025. URL <https://arxiv.org/abs/2506.07902>.

Xie, D., Xu, Z., Hong, Y., Tan, H., Liu, D., Liu, F., Kaufman, A., and Zhou, Y. Progressive autoregressive video diffusion models. In *Proceedings of the Computer Vision and Pattern Recognition Conference*, pp. 6322–6332, 2025.

Yang, L., Liu, S., Meng, T., and Osher, S. J. In-context operator learning with data prompts for differential equation problems. *Proceedings of the National Academy of Sciences*, 120(39):e2310142120, 2023.

Yao, J., Mammadov, A., Berner, J., Kerrigan, G., Ye, J. C., Azizzadenesheli, K., and Anandkumar, A. Guided diffusion sampling on function spaces with applications to pdes, 2025. URL <https://arxiv.org/abs/2505.17004>.

Ye, Z., Huang, X., Chen, L., Liu, H., Wang, Z., and Dong, B. Pdeformer: Towards a foundation model for one-dimensional partial differential equations, 2025a. URL <https://arxiv.org/abs/2402.12652>.

Ye, Z., Zhang, C.-S., and Wang, W. Recurrent neural operators: Stable long-term pde prediction, 2025b. URL <https://arxiv.org/abs/2505.20721>.

Zhou, H., Ma, Y., Wu, H., Wang, H., and Long, M. Unisolver: Pde-conditional transformers towards universal neural pde solvers, 2025. URL <https://arxiv.org/abs/2405.17527>.

Zhou, S., Yang, P., Wang, J., Luo, Y., and Loy, C. C. Upscale-a-video: Temporal-consistent diffusion model for real-world video super-resolution. In *Proceedings of the IEEE/CVF Conference on Computer Vision and Pattern Recognition*, pp. 2535–2545, 2024.

Zhu, M., Sun, J., Zhang, Z., Schaeffer, H., and Lu, L. Pi-mfm: Physics-informed multimodal foundation model for solving partial differential equations, 2025. URL <https://arxiv.org/abs/2512.23056>.

## A. Numerical analysis on error accumulation

### A.1. Deterministic neural operators: geometric compounding

**Setup.** Let  $\Phi : \mathcal{X} \rightarrow \mathcal{X}$  be the true one-step latent dynamics and  $f_\theta : \mathcal{X} \rightarrow \mathcal{X}$  a deterministic learned operator. Rollouts satisfy

$$\mathbf{x}_{n+1}^* = \Phi(\mathbf{x}_n^*), \quad \mathbf{x}_{n+1} = f_\theta(\mathbf{x}_n). \quad (\text{A1})$$

Define  $\delta_n := \mathbf{x}_n - \mathbf{x}_n^*$  and  $e_n := f_\theta(\mathbf{x}_n) - \Phi(\mathbf{x}_n)$ .

**Assumption A.1** (Lipschitz true dynamics).  $\Phi$  is  $L$ -Lipschitz:  $\|\Phi(\mathbf{x}) - \Phi(\mathbf{y})\| \leq L\|\mathbf{x} - \mathbf{y}\|$ .

**Lemma A.2** (Deterministic error recursion). *Under Assumption A.1,*

$$\|\delta_{n+1}\| \leq \|e_n\| + L\|\delta_n\|. \quad (\text{A2})$$

*Proof.* Add and subtract  $\Phi(\mathbf{x}_n)$ :

$$\delta_{n+1} = f_\theta(\mathbf{x}_n) - \Phi(\mathbf{x}_n^*) = e_n + (\Phi(\mathbf{x}_n) - \Phi(\mathbf{x}_n^*)),$$

then apply the triangle inequality and Lipschitzness of  $\Phi$ .  $\square$

**Proposition A.3** (Deterministic compounding bound). *If  $\delta_0 = 0$ , then*

$$\|\delta_n\| \leq \sum_{j=0}^{n-1} L^{n-1-j} \|e_j\|. \quad (\text{A3})$$

*Proof.* Unroll the recursion (A2) by induction.  $\square$

**Interpretation.** When  $L > 1$ , one-step errors are amplified geometrically due to the intrinsic expansiveness of the true dynamics. This amplification is inherited by any deterministic autoregressive rollout.

### A.2. Flow matching with an uncertainty knob: multi-step stability

**Setup** We model  $p(\mathbf{x}_1 \mid \mathbf{x}_0, c)$  by a conditional probability flow trained on the  $k$ -softened source (3):

$$\tilde{\mathbf{x}}_0^k = (1 - k)\mathbf{x}_0 + k\mathbf{z}, \quad \mathbf{z} \sim \mathcal{N}(0, \mathbf{I}). \quad (\text{A4})$$

Bridge states are  $\mathbf{x}_t^k = (1 - t)\tilde{\mathbf{x}}_0^k + t\mathbf{x}_1$  and the sample-wise velocity is  $\mathbf{u}_t^k = (\mathbf{x}_1 - \mathbf{x}_t^k)/(1 - t)$ . The model predicts  $\hat{\mathbf{x}}_1 = \mathbf{g}_\theta(\mathbf{x}_t^k, t, c)$  and induces the velocity

$$\mathbf{v}_\theta(\mathbf{x}, t, c) := \frac{\mathbf{g}_\theta(\mathbf{x}, t, c) - \mathbf{x}}{1 - t}. \quad (\text{A5})$$

At inference, we integrate the PF-ODE

$$\dot{\mathbf{x}} = \mathbf{v}_\theta(\mathbf{x}, t, c), \quad \mathbf{x}(0) = \tilde{\mathbf{x}}_0^k, \quad (\text{A6})$$

from  $t = 0$  to  $t = 1 - \epsilon$  and take  $\hat{\mathbf{x}}_{1-\epsilon}$  as the predicted next latent.

**Ideal transport field.** Let  $\mathbf{v}^*(\mathbf{x}, t, c)$  denote the (unknown) ideal velocity field corresponding to the true conditional transition. We measure model error via the residual

$$\mathbf{r}(\mathbf{x}, t, c) := \mathbf{v}_\theta(\mathbf{x}, t, c) - \mathbf{v}^*(\mathbf{x}, t, c). \quad (\text{A7})$$

**Assumption A.4** (Scaled Lipschitz regularity on the rollout support). Fix  $c$ . On the set of states visited by PF-ODE trajectories initialized from  $\tilde{\pi}_0^k$  (the distribution induced by (A4)), the scaled residual  $(1 - t)\mathbf{r}(\cdot, t, c)$  is Lipschitz in  $\mathbf{x}$  with constant  $L_r(t)$ :

$$\|(1 - t)(\mathbf{r}(\mathbf{x}, t, c) - \mathbf{r}(\mathbf{y}, t, c))\| \leq L_r(t)\|\mathbf{x} - \mathbf{y}\|. \quad (\text{A8})$$

**Assumption A.5** (Ideal field stabilization near  $t \rightarrow 1$ ). Fix  $c$ . The ideal velocity satisfies a one-sided stability bound: there exists  $m(t) \geq 0$  such that for all  $\mathbf{x}, \mathbf{y}$  on the rollout support,

$$\langle \mathbf{x} - \mathbf{y}, \mathbf{v}^*(\mathbf{x}, t, c) - \mathbf{v}^*(\mathbf{y}, t, c) \rangle \leq -\frac{1 - m(t)}{1 - t}\|\mathbf{x} - \mathbf{y}\|^2. \quad (\text{A9})$$

**Remarks on assumptions.** Assumption A.5 is the formal expression of the fact that the probability-flow bridge is *at most weakly expansive* and typically *contractive* as  $t \rightarrow 1$  due to the endpoint parameterization (A5) (the  $1/(1-t)$  factor penalizes deviations near the endpoint). Assumption A.4 is where the uncertainty knob enters: training with  $k > 0$  exposes the model to off-manifold inputs drawn from  $\tilde{\pi}_0^k$ , making Lipschitz control on the rollout support plausible; without  $k$ , such control is not implied by the data distribution.

### A.2.1. A ONE-STEP DEVIATION BOUND (PATHWISE)

Fix  $c$  and  $k$ . Let  $\mathbf{x}(t)$  and  $\mathbf{x}^*(t)$  be PF-ODE solutions driven by  $\mathbf{v}_\theta$  and  $\mathbf{v}^*$  with the same initial condition  $\mathbf{x}(0) = \tilde{\mathbf{x}}_0^k$ . Define  $\Delta(t) := \mathbf{x}(t) - \mathbf{x}^*(t)$ .

**Lemma A.6** (Rescaled Gronwall bound). *Under Assumptions A.4–A.5, for any  $\epsilon \in (0, 1)$ ,*

$$\|\Delta(1-\epsilon)\| \leq \epsilon \exp\left(\int_0^{1-\epsilon} \frac{L_r(t) + m(t)}{1-t} dt\right) \int_0^{1-\epsilon} \frac{\|(1-t)\mathbf{r}(\mathbf{x}^*(t), t, c)\|}{\epsilon(1-t)} dt. \quad (\text{A10})$$

*Proof.* Differentiate  $\Delta$ :

$$\dot{\Delta}(t) = \mathbf{v}^*(\mathbf{x}(t), t, c) - \mathbf{v}^*(\mathbf{x}^*(t), t, c) + \mathbf{r}(\mathbf{x}(t), t, c).$$

Let  $y(t) := \Delta(t)/(1-t)$ . Then

$$\dot{y}(t) = \frac{\dot{\Delta}(t)}{1-t} + \frac{\Delta(t)}{(1-t)^2}.$$

Taking the inner product with  $y(t)$  and using  $\Delta(t) = (1-t)y(t)$  gives

$$\frac{1}{2} \frac{d}{dt} \|y(t)\|^2 = \left\langle y(t), \frac{\mathbf{v}^*(\mathbf{x}(t), t, c) - \mathbf{v}^*(\mathbf{x}^*(t), t, c)}{1-t} \right\rangle + \left\langle y(t), \frac{\mathbf{r}(\mathbf{x}(t), t, c)}{1-t} \right\rangle + \frac{\|y(t)\|^2}{1-t}.$$

Apply Assumption A.5 with  $\Delta = (1-t)y$ :

$$\left\langle y, \frac{\mathbf{v}^*(\mathbf{x}, t, c) - \mathbf{v}^*(\mathbf{x}^*, t, c)}{1-t} \right\rangle \leq -\frac{1-m(t)}{(1-t)} \|y\|^2.$$

Thus the ideal field cancels the singular drift up to  $m(t)$ :

$$\frac{1}{2} \frac{d}{dt} \|y\|^2 \leq \frac{m(t)}{1-t} \|y\|^2 + \left\langle y, \frac{\mathbf{r}(\mathbf{x}(t), t, c)}{1-t} \right\rangle.$$

For the residual term, add and subtract  $\mathbf{r}(\mathbf{x}^*(t), t, c)$  and use Cauchy–Schwarz:

$$\left\langle y, \frac{\mathbf{r}(\mathbf{x}(t), t, c)}{1-t} \right\rangle \leq \frac{\|y\|}{1-t} \|\mathbf{r}(\mathbf{x}^*(t), t, c)\| + \frac{\|y\|}{1-t} \|\mathbf{r}(\mathbf{x}(t), t, c) - \mathbf{r}(\mathbf{x}^*(t), t, c)\|.$$

Using Assumption A.4 and  $\|\Delta\| = (1-t)\|y\|$ ,

$$\|\mathbf{r}(\mathbf{x}(t), t, c) - \mathbf{r}(\mathbf{x}^*(t), t, c)\| \leq \frac{L_r(t)}{1-t} \|\Delta(t)\| = L_r(t) \|y(t)\|.$$

Therefore,

$$\frac{d}{dt} \|y(t)\| \leq \frac{L_r(t) + m(t)}{1-t} \|y(t)\| + \frac{\|\mathbf{r}(\mathbf{x}^*(t), t, c)\|}{1-t}.$$

Apply Gronwall from 0 to  $1-\epsilon$  and use  $y(0) = 0$  (same initial condition):

$$\|y(1-\epsilon)\| \leq \exp\left(\int_0^{1-\epsilon} \frac{L_r(t) + m(t)}{1-t} dt\right) \int_0^{1-\epsilon} \frac{\|\mathbf{r}(\mathbf{x}^*(t), t, c)\|}{1-t} dt.$$

Finally  $\Delta(1-\epsilon) = \epsilon y(1-\epsilon)$  yields (A10). Rewriting  $\|\mathbf{r}\| = \|(1-t)\mathbf{r}\|/(1-t)$  gives the stated form.  $\square$

A.2.2. MULTI-STEP ROLLOUT RECURSION AND THE ROLE OF  $k$ 

We now connect the one-step bound to autoregressive rollouts and isolate the effect of  $k$ .

**Rollout definition.** Let  $\mathbf{x}_s$  be the predicted latents and  $\mathbf{x}_s^*$  the ideal latents under the ideal flow transition. At step  $s$ , the model samples  $\mathbf{z}_s \sim \mathcal{N}(0, \mathbf{I})$  and forms

$$\tilde{\mathbf{x}}_s^k = (1 - k)\mathbf{x}_s + k\mathbf{z}_s, \quad \tilde{\mathbf{x}}_s^{*,k} = (1 - k)\mathbf{x}_s^* + k\mathbf{z}_s, \quad (\text{A11})$$

using the *same*  $\mathbf{z}_s$  for coupling. Let  $\mathcal{T}_\theta^{k,c_s}$  denote the PF-ODE mapping  $t : 0 \rightarrow 1 - \epsilon$  induced by  $\mathbf{v}_\theta(\cdot, t, c_s)$ , and  $\mathcal{T}^{k,c_s}$  the mapping induced by  $\mathbf{v}^*$ . Then

$$\mathbf{x}_{s+1} = \mathcal{T}_\theta^{k,c_s}(\tilde{\mathbf{x}}_s^k), \quad \mathbf{x}_{s+1}^* = \mathcal{T}^{k,c_s}(\tilde{\mathbf{x}}_s^{*,k}).$$

Define  $\delta_s := \mathbf{x}_s - \mathbf{x}_s^*$ .

**Lemma A.7** (Softening contracts the carried-over error). *With the coupling (A11),  $\tilde{\mathbf{x}}_s^k - \tilde{\mathbf{x}}_s^{*,k} = (1 - k)\delta_s$ , hence*

$$\|\tilde{\mathbf{x}}_s^k - \tilde{\mathbf{x}}_s^{*,k}\| = (1 - k)\|\delta_s\|. \quad (\text{A12})$$

**Assumption A.8** (Lipschitzness of the ideal PF transition). For fixed  $c$  and  $k$ , the ideal mapping  $\mathcal{T}^{k,c}$  is  $L_T$ -Lipschitz on the rollout support:

$$\|\mathcal{T}^{k,c}(x) - \mathcal{T}^{k,c}(y)\| \leq L_T\|x - y\|.$$

**Theorem A.9** (Multi-step error recursion for flow matching with knob  $k$ ). *Assume A.4, A.5, and A.8. Let  $B(c_s, k, \epsilon)$  denote the one-step deviation bound from Lemma A.6 evaluated at step  $s$  (i.e., the right-hand side of (A10) with  $c = c_s$ ). Then the rollout error satisfies*

$$\|\delta_{s+1}\| \leq L_T(1 - k)\|\delta_s\| + B(c_s, k, \epsilon). \quad (\text{A13})$$

Consequently, if  $L_T(1 - k) < 1$ ,

$$\|\delta_n\| \leq \sum_{j=0}^{n-1} (L_T(1 - k))^{n-1-j} B(c_j, k, \epsilon). \quad (\text{A14})$$

*Proof.* Add and subtract  $\mathcal{T}^{k,c_s}(\tilde{\mathbf{x}}_s^k)$ :

$$\delta_{s+1} = \mathcal{T}_\theta^{k,c_s}(\tilde{\mathbf{x}}_s^k) - \mathcal{T}^{k,c_s}(\tilde{\mathbf{x}}_s^{*,k}) = \underbrace{\left( \mathcal{T}_\theta^{k,c_s}(\tilde{\mathbf{x}}_s^k) - \mathcal{T}^{k,c_s}(\tilde{\mathbf{x}}_s^k) \right)}_{(\text{I})} + \underbrace{\left( \mathcal{T}^{k,c_s}(\tilde{\mathbf{x}}_s^k) - \mathcal{T}^{k,c_s}(\tilde{\mathbf{x}}_s^{*,k}) \right)}_{(\text{II})}.$$

Term (I) is controlled by Lemma A.6:  $\|(\text{I})\| \leq B(c_s, k, \epsilon)$ . Term (II) is controlled by Assumption A.8 and Lemma A.7:

$$\|(\text{II})\| \leq L_T\|\tilde{\mathbf{x}}_s^k - \tilde{\mathbf{x}}_s^{*,k}\| = L_T(1 - k)\|\delta_s\|.$$

Combine to obtain (A13). Unrolling gives (A14).  $\square$

**Comparison with deterministic rollouts.** Deterministic operators propagate error through the intrinsic Lipschitz constant  $L$  of  $\Phi$  (Proposition A.3). In contrast, flow-matching rollouts satisfy (A13), where the carried-over error is damped by  $(1 - k)$  and the remaining one-step deviation is governed by the learned residual along the PF-ODE (Lemma A.6). Thus,  $k$  is not a cosmetic perturbation: it directly controls the contraction factor  $L_T(1 - k)$  in the multi-step recursion and enlarges the training support to justify Assumption A.4.

## B. Dataset description

All the data are compressed to float16 (half) precision to enable the Data Distributed Parallel training on a 4 H-100 GPU node. The ratio of train:val:test is 8:1:1. Datasets are sampled with equal probabilities according to the practice in DPOT (Hao et al., 2024).

**FNO-v** We upsampled original data from c1p64 to c3p128 (the 2nd and 3rd dimension are filled with zero). The dataset size is expanded from 11.1GB to 21GB. Trajectory count: FNO-v5 – 15.4k, FNO-v4 – 368k, FNO-v3 – 184k.

**PDEArena** For the PDEArena-NavierStokes(PA-NS) and PDEArena-NavierStokesCond(PA-NSC), the dataset size is compressed from 60GB to 25GB. For the PDEArena-ShallowWaterEquation(PA-SWE), it was slightly expanded to 62GB from 76.6GB because additional all-zero channels are provided. Trajectory count: PA-NS – 48k, PA-NSC – 120k, PA-SWE – 470k.

**PDEBench** For the PDEBench-CompressibleNavierStokes(PB-CNS), unimportant physical fields are filtered. Thus, it becomes 65GB compressed from 551GB. For the PDEBench-ShallowWaterEquation(PB-SWE), it is compressed to 0.3GB from 6.2GB, the 2nd and 3rd dimension is filled with zero. Trajectory count: PB-CNS – 598k, PB-SWE – 77.6k.

**The Well** For the Well-GrayScott(W-GS), we fill the 3rd dimension with zero, ending up with a 5.3GB data set compressed from 153GB. For the Well-ActiveMatter(W-AM), we downsampled the data from c3p256 to c3p128, and obtained a compressed 1.1GB dataset from 51.3GB. For the Well-PlanetShallowWaterEquation(W-SWE), we downsampled the data from c3p256,512 to c3p128 and filtered out unimportant fields, so the data size is compressed to 9.3GB from 185.8GB. For the Well-RayleighBenard(W-RB), we downsampled the data from c3p512,128 to c3p128, and get a 26GB dataset from 342GB original data. For the Well-ShearFlow(W-SF), it is compressed to 14GB from 547GB by filtering out unimportant fields. For the Well-TurbulentRadiativeLayer2D(W-TR), it is downsampled from c3p128,384 to c3p128, thus compressed to 0.5GB from 6.9GB. For the Well-ViscoElasticInstability(W-VE), it is downsampled from c3p512 to c3p128, thus compressed to 0.5GB from 66GB. Trajectory count: W-GS – 92.2k, W-AM – 13.4k, W-SWE – 96.4k, W-RB – 266.6k, W-SF – 175.6k, W-TR – 7k, W-VE – 5.3k.

## C. Model Architectures Details

### C.1. Latent Generative Solvers

P2VAE’s AdamW optimizer is used with  $\beta_1 = 0.9$  and  $\beta_2 = 0.995$ , cosine learning rate schedule with 10% of linear warm up, and a weight decay of 1e-4; PFFT’s AdamW optimizer is used with  $\beta_1 = 0.9$  and  $\beta_2 = 0.95$ , cosine learning rate schedule with 10% of linear warm up, and a weight decay of 1e-4. Base learning rates of 1e-4 for a 256 batch size are adjusted linearly to batch sizes to balance convergence speed and training stability.

We stack 12 layers of SiT unit in each FFT and 12 heads of attention, given embedding dimension 768 (without further notice, we accompany 1 head per 64 model dimension). LGS has 138M parameter, with a dedicated 1.334GFLOPs per sample, regardless of the latent encoding process which is precomputed.

### C.2. Baselines

All baseline methods are trained with 200k steps, with same optimizer configuration as LGS. On the model side, CNextUNet utilize internal dimension 192, with standard ConvNext block and UNet connections, mounting up to 153M with 17.61GFLOPs per sample. U-AFNO shares the same UNet connection, yet concatenate 16 layers of AFNO blocks, with embedding dimension 1024 and Fourier keep mode 64 in the lowest resolution. U-AFNO has 152M parameter, utilziing 90.305GFLOPs per sample. We implement DPOT with patch embedding (patch size 8) and transposed convolution layer to have a lower dimension token counts internally, where Fourier channel mixing (keeping 64 modes) replaces the self-attention; 16 layers of DPOT unit are stacked, given embedding dimension 1024. DPOT has 160M parameter and 103.224 GFLOPs per sample.

### C.3. Ablation Studies

Below we restate each ablation using the conditional objectives  $p(\mathbf{x}_{s+1} \mid \cdot)$  consistent with Sec. 3.

**A1: No pyramids.** Same modeling objective as the full method, but conditioning uses the full-resolution history (no temporal downsampling), increasing attention cost.

$$p(\mathbf{x}_{s+1} \mid \tilde{\mathbf{x}}_s, t, c) p(c \mid \hat{\mathbf{x}}_{1:s}) \quad (\text{A15})$$

where  $\tilde{\mathbf{x}}_s$  is a  $k$ -softened  $\mathbf{x}_s$  at intermediate transport time  $t$ .

**A2: No physics context maintenance.** We remove the latent dynamics variable  $c_s$  and condition directly on noisy history tokens and time marker:

$$p(\mathbf{x}_{s+1} \mid \hat{\mathbf{x}}_s, \hat{\mathbf{x}}_{1:s}, t), \quad (\text{A16})$$

where  $\hat{\mathbf{x}}_{1:s}$  are generated from  $k$ -softened  $\mathbf{x}_{0:s-1}$  in Eq. (3).

**A3: No uncertainty knob  $k$ .** We set  $k = 0$  in Eq. (3) but the rest remains the same as Equation (A16).

**A4: No generative solver.** We replace generative prediction with direct regression:

$$\hat{\mathbf{x}}_{s+1} = f(\mathbf{x}_{0:s}), \quad \min_{\theta} \mathbb{E}[\|\hat{\mathbf{x}}_{s+1} - \mathbf{x}_{s+1}\|_2^2]. \quad (\text{A17})$$

Operation-wise, to ablate temporal pyramids, we remove the state interpolation step before computing, which results in a 4-times rise of GFLOPs, provides marginal gain the model performance. To remove the physics context maintenance, we concatenate predicted states and apply cross-attention onto current state embeddings, which assembles the Perceiver approach (Jaegle et al., 2021). Removing  $k$  knob is convenient, simply mute  $k$  during intermediate states synthesis during training. To reduce our model to non-generative model, we continue using Perceiver, and no longer sample diffusion time but only regress the predicted next state given un-transported current state, which is effectively one-step supervision in x-pred target.

## D. Visualization for test sets of 15 PDE systems

FNO-v: sampled trajectories are displayed in Fig. E1.

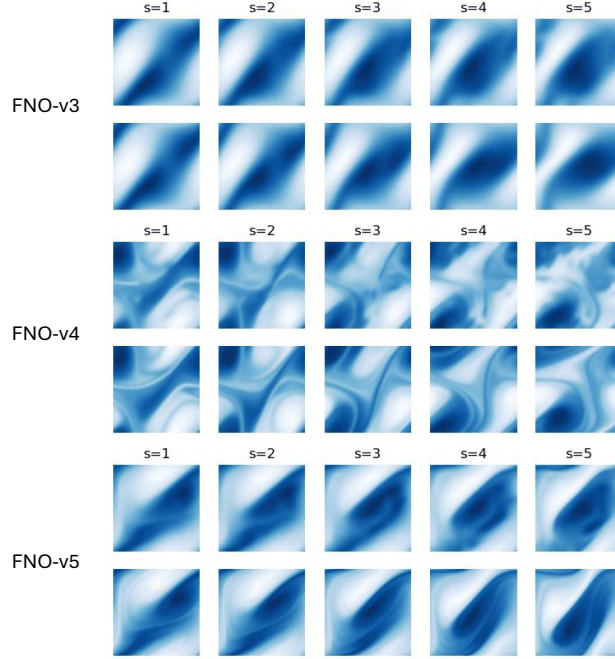


Figure E1. Sampled trajectories from FNO-v3, FNO-v4, FNO-v5. Upper row: prediction. Bottom row: ground truth.

PDEArena: sampled trajectories are displayed in Fig. E2.

PDEBench: sampled trajectories are displayed in Fig. E3.

The Well: sampled trajectories are displayed in Fig. E4.

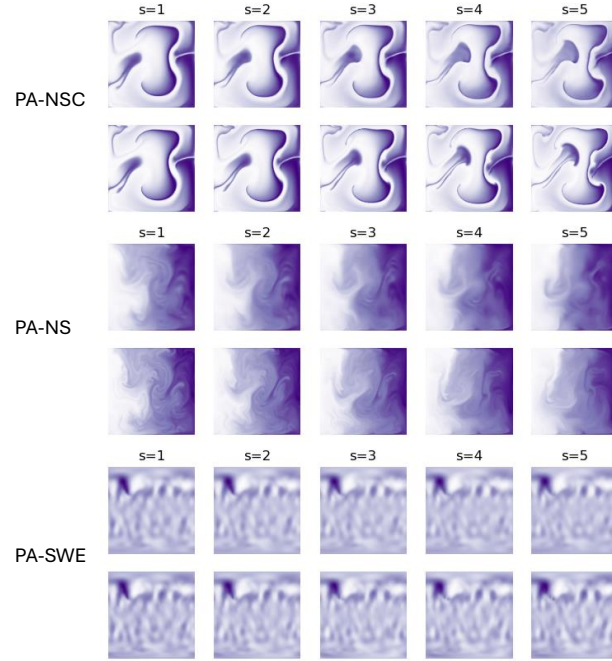


Figure E2. Sampled trajectories from PA-NSC, PA-NS, PA-SWE. Upper row: prediction. Bottom row: ground truth.

## E. Rollout visualizations

Sampled long-term rollout trajectories are provided in Fig. G1 (P-NS), Fig. G2 (PB-CNS-L) and Fig. G3 (PB-CNS-H).

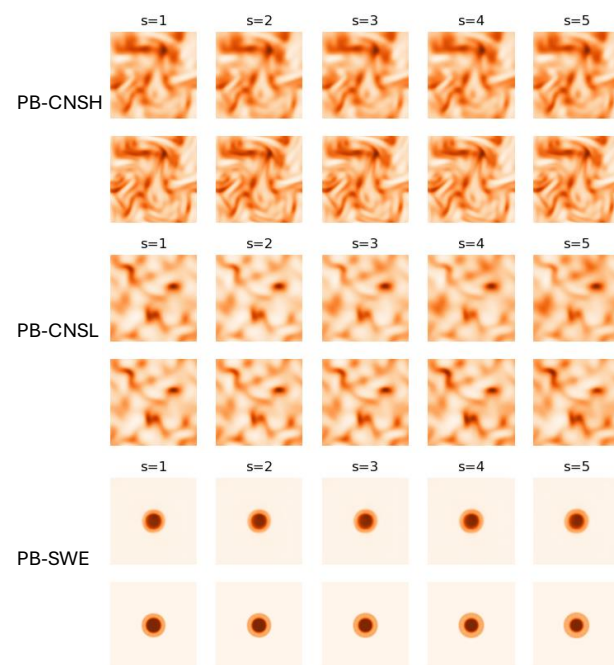


Figure E3. Sampled trajectories from PB-CNSH, PB-CNSL, PB-SWE. Upper row: prediction. Bottom row: ground truth.

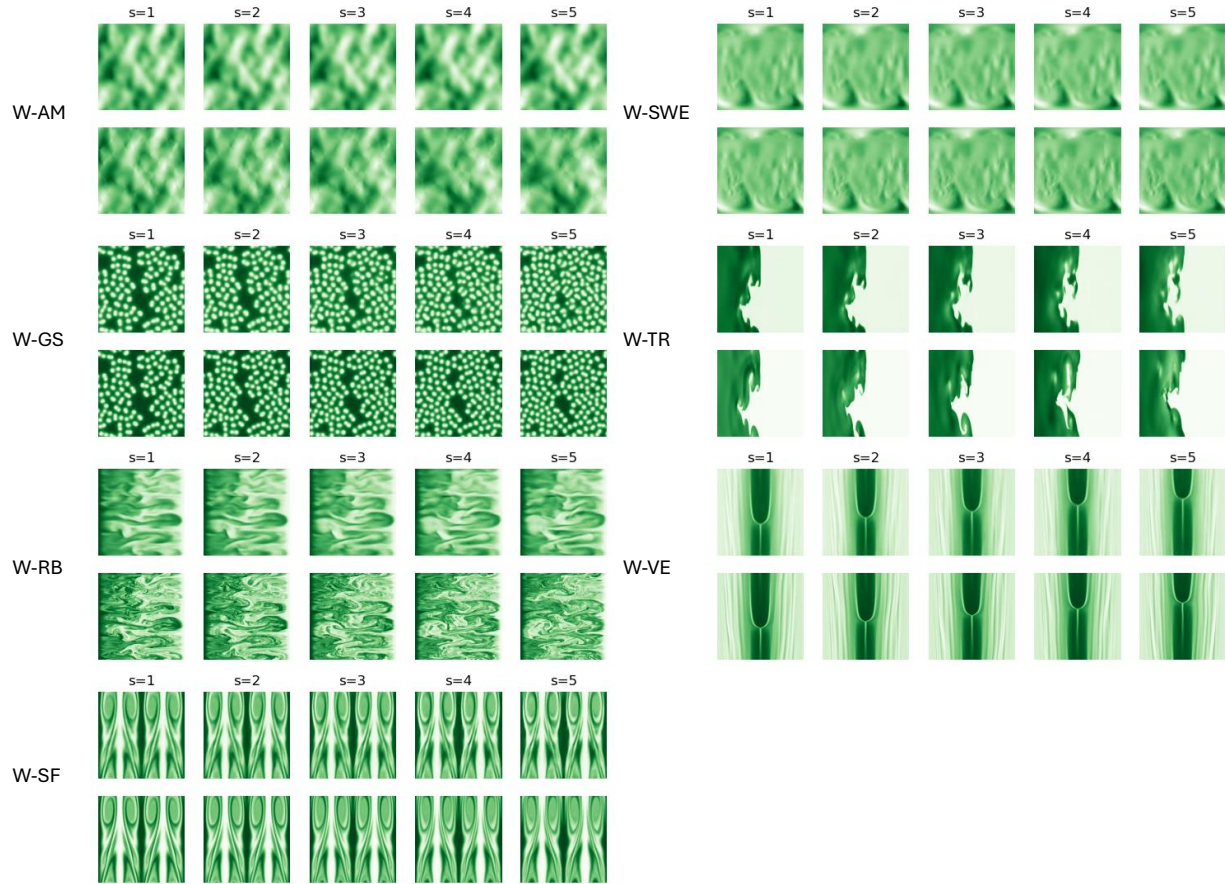


Figure E4. Sampled trajectories from W-AM, W-GS, W-RB, W-SF, W-SWE, W-TR, W-VE. Upper row: prediction. Bottom row: ground truth.

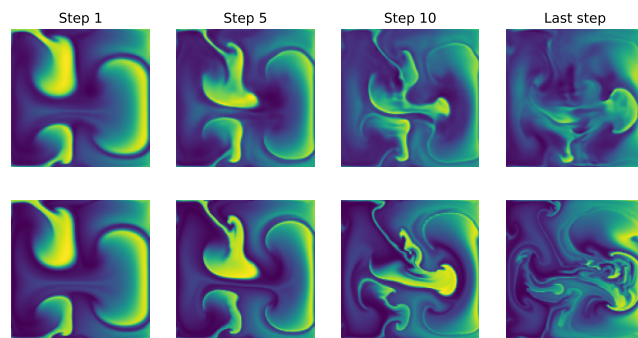


Figure G1. Sampled long-term rollout trajectories from PDEArena-NS by FMT-B-42M. Upper row: prediction. Bottom row: ground truth.

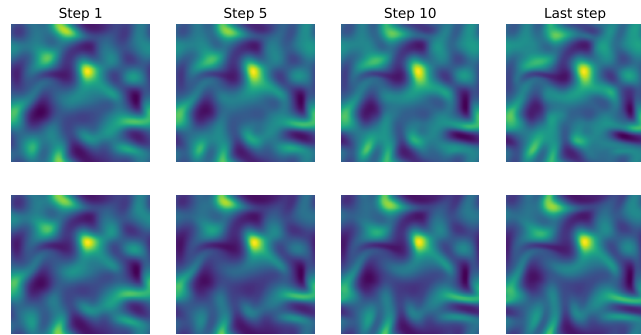


Figure G2. Sampled long-term rollout trajectories from PDEBench-CNS-Low by FMT-B-42M. Upper row: prediction. Bottom row: ground truth.

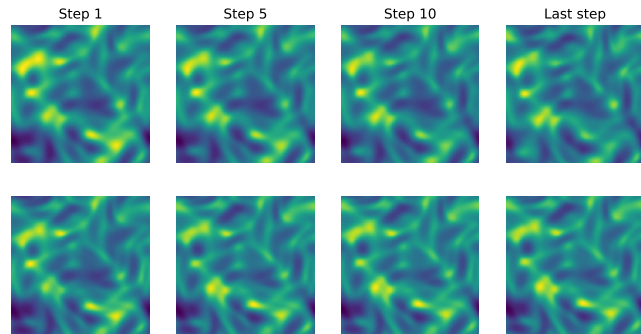


Figure G3. Sampled long-term rollout trajectories from PDEBench-CNS-High by FMT-B-42M. Upper row: prediction. Bottom row: ground truth.